

Model-based, one-sided, time-of-flight terahertz image reconstruction

Stephen M. Schmitt^a, Jeffrey A. Fessler^a, Greg D. Fichter^b, and David A. Zimdars^b

^aEECS Dept., Univ. of Michigan, 1301 Beal Avenue, Ann Arbor, MI 48109;

^bPicometrix LLC, 2925 Boardwalk Dr., Ann Arbor, MI 48104

ABSTRACT

In the last decade, terahertz-mode imaging has received increased attention for non-destructive testing applications due to its ability to penetrate many materials while maintaining a small wavelength. This paper describes a model-based reconstruction algorithm that is able to image defects in the spray-on foam insulation (SOFI) used in aerospace applications that has been sprayed on a reflective metal hull. In this situation, X-ray based imaging is infeasible since only one side of the hull is accessible in flight.

This paper models the object as a grid of materials, each section of which has a constant index of refraction. The delay between the transmission and reception of a THz pulse is related to the integral of the index of refraction along the pulse's path, and we adapt computed tomography (CT) methods to reconstruct an image of an object's index of refraction.

We present the results of our reconstruction method using real data of the timing of THz pulses passing through a block of SOFI with holes of a known location and radius. The resulting image of the block has a low level of noise, but contains artifacts due to the limited angular range of one-sided imaging and due to the narrow beam approximation used in the forward model.

Keywords: Inverse problems, Model-based imaging, Nondestructive testing and evaluation, Computed tomography, Terahertz imaging

1. INTRODUCTION

1.1 Terahertz Imaging

Terahertz-mode imaging is a relatively new technique that has become more accessible due to advances in both ultrafast lasers and optoelectronics^{1,2} that provide the ability to generate and detect single-cycle terahertz pulses. Terahertz imaging is increasingly used for applications including the non-destructive evaluation (NDE) of thermal protection systems for aerospace applications, such as the spray-on foam insulation (SOFI) used by NASA on the exterior of the Space Shuttle. In this situation, other common NDE methods may be unfeasible; for example, X-ray CT imaging or other terahertz CT methods³ would require access to both sides of the SOFI. Terahertz imaging also brings advantages other than this flexibility; the high frequency of terahertz provides a resolution that other RF reflectometry methods are unable to achieve. In addition, the physical imaging system is easy to use, works at a high speed, and can generate and detect pulses synchronously at a high signal-to-noise ratio. Ultrafast terahertz pulses are wideband, allowing wideband spectral analysis of an object; however, in our application we note that the index of refraction of SOFI does not change appreciably over this band.

In our specific application, we have physical access to only one side of the SOFI, but behind the SOFI is a metal reflecting plane. Previous one-sided terahertz imaging methods have used pulses to capture single reflective views in a method similar to an ultrasound B-scan.⁴ This method is limited to imaging laminar structures that present clear specular reflections from each interface. Additionally, features may lie in the shadow of an existing

Further author information: (Send correspondence to S.M.S.)

S.M.S.: E-mail: smschm@umich.edu

J.A.F.: E-mail: fessler@umich.edu

G.D.F.: E-mail: gfichter@picometrix.com

D.A.Z.: E-mail: dzimdars@picometrix.com

defect that scatters terahertz radiation. Another method has been developed that models the object under consideration as a grid of reflective points, and the reflection is measured at an array of angles.^{5,6} This method is able to image interfaces other than those that present a specular reflection. Since SOFI has a low index of refraction, the contrast using this model is low. The specific features that our system is designed to image are holes in the foam, which may be caused by impact from debris or manufacturing defects. These voids will have a lower index of refraction than the SOFI.

This paper describes a system for reconstructing 2D images of the index of refraction of a region with a reflective plane behind it by applying model-based image reconstruction (MBIR) techniques. In general, MBIR is a class of image reconstruction techniques that use model the observed data as a function of underlying image data and estimate the image from the observed data by solving an inverse problem. MBIR methods have been used for many imaging modalities such as CT^{7,8} and MRI^{9,10} to improve artifact and noise properties relative to traditional image reconstruction methods.

In this case, we model the expected time-of-flight of terahertz pulses given an object's index of refraction as a function of space, using a system model similar to that used in computed tomography (CT) problems; we then invert the model to find the index of refraction image. Figure 1 shows the experimental setup. Our data acquisition apparatus relies on a transmitter and receiver moving to acquire data at multiple angles. However, it is clear from the setup that the transmitter and receiver are physically limited to a somewhat narrow angular range, on one end by the foam itself and on the other end by each other. These limitations of the acquisition correspond to a severely limited-angle CT; traditional CT reconstruction algorithms fare poorly in this condition, whereas MBIR is more promising.^{11,12}

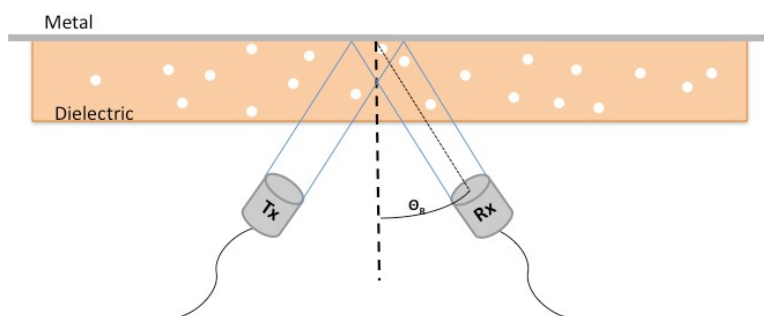


Figure 1. Experimental setup.

Section 2 describes the model we use, shows how this model reduces the image reconstruction problem to a convex optimization problem, and specifies how we perform this optimization. It also describes the apparatus used to collect the data. Section 3 describes how we preprocess the raw data, consisting of time-series received pulses, into time-of-flight data to reconstruct using the methods of Section 2. Section 4 demonstrates the results of our methods using real data collected from SOFI with known holes drilled into it.

2. METHODS

2.1 Model

Our model approximates the index of refraction of an object as a function of space, $n(\vec{x})$, by the weighted sum of several basis functions $R_j(\vec{x})$, $j = 1, \dots, N_{\text{pixel}}$:

$$n(\vec{x}) = \sum_{j=1}^{N_{\text{pixel}}} n_j R_j(\vec{x}).$$

This allows us to represent the (unknown) index of refraction image as a finite-dimensional vector \mathbf{n} . The basis functions we use are square pixels with edge size Δ and centers \vec{x}_j :

$$R_j(\vec{x}) = \text{rect}_2 \left(\frac{\vec{x} - \vec{x}_j}{\Delta} \right),$$

where $\text{rect}_2(\vec{x}) = \mathbf{1}_{\{x_1 \in [-1/2, 1/2]\}} \mathbf{1}_{\{x_2 \in [-1/2, 1/2]\}}$. The i th recorded measurement T_i is related to the travel time of a pulse along a path \mathcal{P}_i , $i = 1, \dots, N_{\text{pulse}}$. We assume that the effect of refraction is negligible, that is, that the paths \mathcal{P}_i that pulses travel along can be determined in advance and are not affected by $n(\vec{x})$. Since SOFI has a low n , this approximation is acceptable. The time it takes a pulse to travel along \mathcal{P}_i is given by the integrated delay of the wave propagation:

$$T_i = \int_{\mathcal{P}_i} \frac{n(\vec{x})}{c} d\vec{x} = \sum_j \frac{n_j}{c} \left(\int_{\mathcal{P}_i} R_j(\vec{x}) d\vec{x} \right). \quad (1)$$

Defining the path length of \mathcal{P}_i through a pixel R_j , divided by c , as a_{ij} :

$$a_{ij} \triangleq \frac{1}{c} \int_{\mathcal{P}_i} R_j(\vec{x}) d\vec{x},$$

then (1) becomes the matrix equation

$$\mathbf{T} = \mathbf{A}\mathbf{n},$$

where $\mathbf{A} \in \mathbb{R}^{N_{\text{pulse}} \times N_{\text{pixel}}}$ represents a system matrix.

In practice we do not observe time delays T_i directly, but T_i shifted by an unknown offset k that depends on the angle of the observation, θ_i . Therefore, we define our model for a delay observation y_i to be:

$$y_i = \left(\sum_{j=1}^{N_{\text{pixel}}} a_{ij} n_j \right) + k(\theta_i) + \epsilon_i, \quad (2)$$

The noise added to the i th observation, ϵ_i , is assumed to be normally distributed and that each observation's noise is identically distributed and independent, so that the covariance matrix of ϵ is $\sigma^2 \mathbf{I}$. The model can be written in a matrix form:

$$\mathbf{y} = \mathbf{A}\mathbf{n} + \mathbf{K}\mathbf{k} + \epsilon, \quad (3)$$

where \mathbf{k} is a vectorization of $k(\theta_i)$ which has a number of elements equal to the number of observation angles N_θ , and $\mathbf{K} \in \mathbb{R}^{N_{\text{pulse}} \times N_\theta}$ is a matrix that expands \mathbf{k} into the number of observations; $[\mathbf{K}]_{im} = 1$ if observation i is taken at the angle corresponding to \mathbf{k}_m and otherwise zero.

The addition of $\mathbf{K}\mathbf{k}$ into the model introduces limitations in the reconstruction. For any image \mathbf{n} that consists of lines of constant n perpendicular to the reflecting backplane, there exists a vector \mathbf{k} such that $\begin{bmatrix} \mathbf{n}^T & \mathbf{k}^T \end{bmatrix}^T$ is in the nullspace of $\begin{bmatrix} \mathbf{A} & \mathbf{K} \end{bmatrix}$, and so the model cannot discern between these features and an offset in \mathbf{k} . In particular, adding a constant to \mathbf{n} becomes undetectable, so the reconstruction can at best produce images of \mathbf{n} up to an unknown constant shift. For our imaging goals, however, this is not a significant limitation.

2.2 Regularization

Since (3) is an underdetermined system, we cannot solve for an image \mathbf{n} from observations \mathbf{y} without adding other prior information. Therefore, we add a prior assumption that larger differences between neighboring pixels are more improbable than smaller ones. We define a differencing matrix $\mathbf{C} \in \mathbb{R}^{N_{\text{diff}} \times N_{\text{pixel}}}$ such that for an image \mathbf{n} , $\mathbf{C}\mathbf{n}$ is a vector containing the difference between each neighboring* pair of pixels in \mathbf{n} . Our regularizer is defined as

$$R(\mathbf{x}) = \sum_{k=1}^{N_{\text{diff}}} \psi([\mathbf{C}\mathbf{x}]_k), \quad (4)$$

where ψ is a Huber function, which is quadratic until a cutoff point, at which the function becomes linear:

$$\psi(x) = \begin{cases} x^2/2, & |x| \leq \delta \\ \delta|x| - \delta^2/2, & |x| > \delta. \end{cases} \quad (5)$$

*We use the definition of a pixel's "neighbors" as the four that touch it on an edge, but other choices could be made, such as including the four that touch it on a corner, or even larger "neighborhoods".

The cutoff point δ is a parameter of the reconstruction. Lower values of δ are better at preserving edges in the reconstruction, but the reconstruction algorithm will take more iterations to converge. The “units” of δ are the same as the “units” of \mathbf{n} , a unitless index of refraction. To preserve the edge between regions with a difference in index of refraction of Δ_n , one might set δ to be approximately $\Delta_n/10$. In our reconstructions, $\delta = 10^{-4}$.

2.3 Reconstruction

Using this regularizer, we reconstruct the index of refraction image \mathbf{n} and simultaneously estimate the nuisance delay parameter \mathbf{k} by finding the minimizer of the following cost function:

$$\hat{\mathbf{n}}, \hat{\mathbf{k}} = \operatorname{argmin}_{\mathbf{n}, \mathbf{k}} \Psi(\mathbf{n}, \mathbf{k})$$

$$\Psi(\mathbf{n}, \mathbf{k}) \triangleq \frac{1}{2} \|\mathbf{y} - \mathbf{A}\mathbf{n} - \mathbf{K}\mathbf{k}\|_2^2 + \beta R(\mathbf{n}). \quad (6)$$

Since Ψ is a convex function, it has a unique minimizer. Of the many possible algorithms for performing minimization, we used a preconditioned conjugate gradient algorithm.¹³

2.4 Implementation

Computation of the product $\mathbf{A}\mathbf{n}$ requires computation of each matrix element a_{ij} , which is not straightforward. However, we leverage existing algorithms for CT projection to accomplish this computation. If there were no reflective backing, and the transmitter simply sent a pulse through an object, non-refracted, directly to a receiver that measured the pulse’s time-of-flight, then the system would be measuring line integrals of n along straight paths through the object. Model-based reconstruction for CT already relies on algorithms for computing these straight-line integrals, or *projections*, of the image. If we define our coordinate system such that the reflector is at the line $x_2 = 0$ and the object is in the region where $x_2 > 0$, we can define an operator \mathcal{R} that duplicates a reflection of the image $n(\vec{x})$ behind the reflector:

$$(\mathcal{R}n)(x_1, x_2) = n(x_1, |x_2|)$$

We can then compute the system matrix as:

$$a_{ij} = \frac{1}{c} \int_{\mathcal{R}\mathcal{P}_i} (\mathcal{R}R_j)(\vec{x}) d\vec{x},$$

where $\mathcal{R}\mathcal{P}_i$ is the path \mathcal{P}_i with one half (either half is equivalent) reflected across the reflective surface. When defined this way, \mathbf{A} is simply a CT system matrix. Figure 2 shows the effect of \mathcal{R} on the regions R_j and its straightening of the path \mathcal{P}_i .

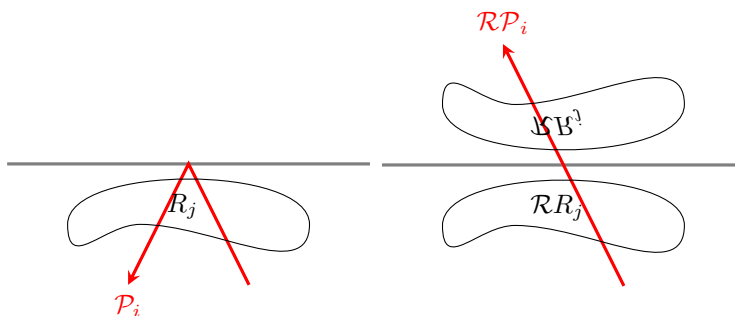


Figure 2. Reflection \mathcal{R} of R_j and \mathcal{P}_i .

2.5 Experimental Apparatus

Figure 1 shows a diagram of the experimental apparatus used to collect data, and Figure 3 shows a picture of the apparatus. It consists of a terahertz transmitter and receiver mounted together with a scissoring mechanism that keeps them both at the same angle (denoted θ on Figure 1) relative to a center line that is kept perpendicular to the reflective backing. The sample moves with respect to the transmitter and receiver heads on a linear gantry parallel to the reflective backing. To collect the pulse data, the scissor mechanism fixes the heads at a given angle and then the gantry moves continuously, transmitting pulses at a fixed rate. As shown in Figure 1, each pulse travels through the dielectric SOFI, reflects off the metal backing, and travels through the dielectric again. After the sample traverses along the gantry once at a given angle, the heads increase their angle by $\Delta\theta$ and the sample traverses again. After the data for N_θ angles is collected, the scan is complete; the apparatus has collected a received pulse at each angle and each linear offset location.

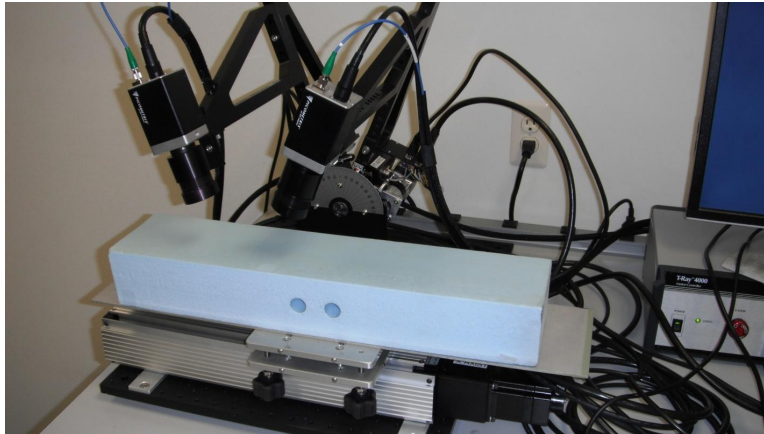


Figure 3. Picture of experimental apparatus.

3. DATA PROCESSING

3.1 Peak Finding

The output of the experimental apparatus is not delays, but discrete-time measured pulses $x_i[n]$, $n = 0, \dots, 4095$. If we have a reference pulse $r[n]$, to find the delay between the reference pulse and a measured pulse $x[n]$, we find the delay d that maximizes a fit function

$$\Phi(d; r, x) = \sum_n x[n](\mathcal{D}(d)r)[n],$$

where $\mathcal{D}(d)$ is an operator that delays a pulse (shifts it forward in time) by d samples. Since we would like to be able to resolve the value of d to a precision less than the size of a time step, we use the discrete Fourier transform of r to define its non-integer shift. If $R[k]$ is the DFT of r , the DFT of r shifted forward in time by d samples is:

$$R_d[k] = R[k] \exp(-j2\pi kd/N),$$

and the inverse Fourier transform of $R_d[k]$ is $\mathcal{D}(d)r$. Since $x[n]$ is real, we use the Plancherel theorem to quickly compute Φ using $X[k]$, the DFT of x :

$$\Phi(d; r, x) \propto \sum_k X^*[k]R_d[k] = \sum_k X^*[k]R[k] \exp(-j2\pi kd/N).$$

To find the delay d that maximizes Φ , we first find Φ for each integral d from the inverse DFT of $X^*[k]R[k]$. Define d_{imax} to be the integral d that maximizes Φ . We maximize Φ for non-integral d by performing a binary search to find a zero in its derivative in the interval $[d_{\text{imax}} - 1, d_{\text{imax}} + 1]$.

3.2 Determining a Reference Pulse

We find the reference pulse r from pulses measured with no object present. We make the assumption that, for a fixed angle, the no-object (or “blank”) pulse should be the same regardless of the translation position, except for a delay. We assume that this delay for a particular angle θ and translation position s , which we define $d_{\theta,s}$, is intrinsic to the acquisition mechanism, and will remain constant between the data acquisition for no object present and with an object.

Define the blank pulse at an angle θ and translation position s as $b_{\theta,s}[n]$. First, we find the average of all N_s blank pulses for a given angle, which we define

$$\bar{b}_\theta[n] = \frac{1}{N_s} \sum_s b_{\theta,s}[n].$$

Since the delay for changing translation position is small, this average is an estimate of the reference pulse but will be blurred. We then estimate the intrinsic delay $d_{\theta,s}$ for each s as

$$d_{\theta,s} = \operatorname{argmin}_d \Phi(d; b_{\theta,s}, \bar{b}_\theta)$$

and using these delays, form our reference pulse $r_\theta[n]$ for an angle θ :

$$r_\theta = \frac{1}{N_s} \sum_s \mathcal{D}(d_{\theta,s}) b_{\theta,s}.$$

Since the pulses are now aligned before being averaged, our reference pulse will be sharper for the object scan data.

3.3 Processing the Scanned Object

With a reference pulse determined, we process the data acquired with an object present. Define $p_{\theta,s}[n]$ to be the pulse measured at angle θ and translation s , with an object present. The delay of this pulse, which we define $y_{\theta,s}$, can be found as:

$$y_{\theta,s} = d_{\theta,s} + \operatorname{argmin}_d \Phi(d; r_\theta, p_{\theta,s}).$$

We assemble all measurements $y_{\theta,s}$ into an observation vector \mathbf{y} and proceed with reconstruction from (3).

4. RESULTS

To evaluate our methods, we acquired data using several blocks of SOFI with holes drilled in them. In all tests, the block of SOFI was 76.2mm thick and the holes drilled through it had a diameter of 19.05mm. The gantry moved continuously and pulsed the transmitter every 0.01 seconds; each 10 pulses were binned together and averaged in lateral steps of $\Delta_s = 1\text{mm}$. The collected angles of incidence θ ranged from 10 to 50 degrees in $\Delta_\theta = 2$ degree increments. The time sampling interval of the receiver was 78.125 femtoseconds.

The reconstruction was made with a pixel size of $\Delta = 2.5\text{mm}$, a regularization parameter of $\beta = 2^9$, a Huber cutoff of $\delta = 10^{-4}$, and 500 iterations of our preconditioned conjugate gradient algorithm.

There were two series of acquisitions: in the first, the block only had one hole drilled in it. We acquired data with the hole in three positions; once in the center (38.1mm from the reflector), once translated 15mm toward the front of the block (53.1mm from the reflector), and once translated 15mm toward the back (23.1mm from the reflector). Figure 4 shows the delays produced when the hole is in the center of the block; the pulse speed-up caused by both the hole and its reflection are visible at each angle. Figure 5 shows the images produced from these acquisitions. In the second series of acquisitions, two holes were drilled in the SOFI, placed with their centers 40mm and 30mm apart, respectively, to determine how close two features can be placed while resolving them. The hole separation was parallel to the reflecting plane, both holes were centered in the depth axis, 38.1mm from the reflector. Figure 6 shows the images produced with two holes. The material used had an index of refraction separately measured as 1.016.

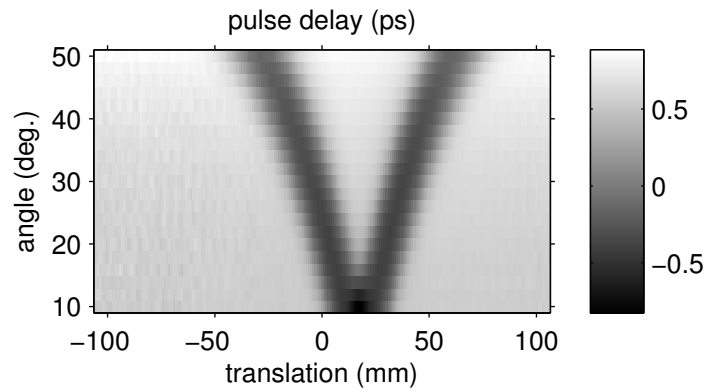


Figure 4. Centered hole delays.

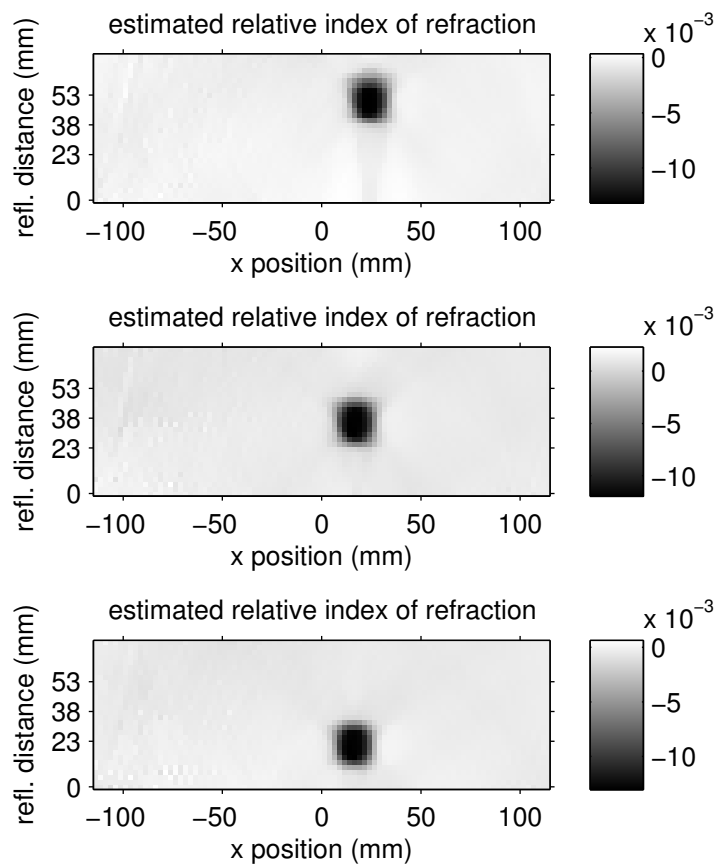


Figure 5. Reconstruction of one-hole images; (top) with hole 15mm toward front, (center) with hole centered, (bottom) with hole 15mm toward back.

5. CONCLUSIONS

The methods presented work successfully to image large defects in SOFI, with the major artefacts in the reconstructed images being the blurry edges of the holes and the artifactual region of high index of refraction between two holes. We believe that the blurry edges of the holes are a result of the width (perpendicular to its direction of travel) of the terahertz pulse. We attempted to reconstruct the images with a simple model that accounts for this pulse width, but it did not improve the images compared to the described model that uses zero pulse width. We are unsure of the origin of the artifacts between the holes.

As mentioned when describing our model, the presence of the \mathbf{Kk} term improves the quality of the reconstruction at the expense of rendering certain effects not reconstructable. Figure 7 shows the reconstruction of the center hole (as in the middle subfigure of Figure 5) without this correction term. For our application, this notably includes a constant term over the image, meaning that our images are of index of refraction minus a constant, which is reflected in the scale of the images. The reconstruction correctly estimates that the SOFI has an index of refraction approximately 0.015 greater than that of air, but does not estimate the actual index of refraction. Secondly, our model cannot find the front of the SOFI block if it is parallel to the reflecting plane, which it was in our experiments. We assume that in practice, the nominal depth of the SOFI is known, and in our reconstructions we limit the depth of the reconstruction to the depth of the SOFI to eliminate this concern. Even with the depth of the SOFI known, the constant term in the images cannot be corrected. More concerningly, a gap of air in the SOFI that is large in the direction parallel to the reflector but small in the opposing direction may be weakly detectable; however, this is a great situation for scattering terahertz tomography, which could complement our index of refraction tomography.

This method could be extended to 3D tomography by applying the data collection in several parallel planes and then simultaneously minimizing the data-fit penalty in each plane and a 3D regularizer. This would likely produce better 3D images than ones constructed by using our method on several 2D planes independently, since the influence of the 3D regularizer allows structural information in one plane to propagate to other planes.

ACKNOWLEDGMENTS

This work was supported in part by NASA STTR grant T7.01-9931 and hardware donations from the Intel Corporation.

REFERENCES

- [1] Smith, P. R., Auston, D. H., and Nuss, M. C., "Subpicosecond photoconducting dipole antennas," *Quantum Electronics, IEEE Journal of* **24**(2), 255–260 (1988).
- [2] Fattinger, C. and Grischkowsky, D., "Terahertz beams," *Applied Physics Letters* **54**(6), 490–492 (1989).
- [3] Ferguson, B., Wang, S., Gray, D., Abbot, D., and Zhang, X.-C., "T-ray computed tomography," *Optics Letters* **27**(15), 1312–1314 (2002).
- [4] Mittleman, D. M., Hunsche, S., Boivin, L., and Nuss, M. C., "T-ray tomography," *Optics letters* **22**(12), 904–906 (1997).
- [5] Musheinessh, M. A., Divin, C. J., Fessler, J. A., and Norris, T. B., "Time-reversal and model-based imaging in a thz waveguide," in [*Conference on Lasers and Electro-Optics*], Optical Society of America (2009).
- [6] Musheinessh, M. A., Divin, C. J., Fessler, J. A., and Norris, T. B., "Model-based thz imaging for 2d reflection-mode geometry," in [*2010 Conference on Lasers and Electro-Optics (CLEO) and Quantum Electronics and Laser Science Conference (QELS)*], 1–2, IEEE (2010).
- [7] Wang, G., Vannier, M. W., and Cheng, P. C., "Iterative X-ray cone-beam tomography for metal artifact reduction and local region reconstruction," *Microscopy and Microanalysis* **5**, 58–65 (Jan. 1999).
- [8] De Man, B., Nuyts, J., Dupont, P., Marchal, G., and Suetens, P., "An iterative maximum-likelihood polychromatic algorithm for CT," *IEEE Trans. Med. Imag.* **20**, 999–1008 (Oct. 2001).
- [9] Sutton, B. P., Noll, D. C., and Fessler, J. A., "Fast, iterative image reconstruction for MRI in the presence of field inhomogeneities," *Medical Imaging, IEEE Transactions on* **22**(2), 178–188 (2003).
- [10] Block, K. T., Uecker, M., and Frahm, J., "Undersampled radial MRI with multiple coils. iterative image reconstruction using a total variation constraint," *Magnetic resonance in medicine* **57**(6), 1086–1098 (2007).

- [11] Andersen, A. H., "Algebraic reconstruction in CT from limited views," *IEEE Trans. Med. Imag.* **8**, 50–5 (Mar. 1989).
- [12] Delaney, A. H. and Bresler, Y., "Globally convergent edge-preserving regularized reconstruction: an application to limited-angle tomography," *IEEE Trans. Im. Proc.* **7**, 204–21 (Feb. 1998).
- [13] Fessler, J. A. and Booth, S. D., "Conjugate-gradient preconditioning methods for shift-variant PET image reconstruction," *IEEE Trans. Im. Proc.* **8**, 688–99 (May 1999).

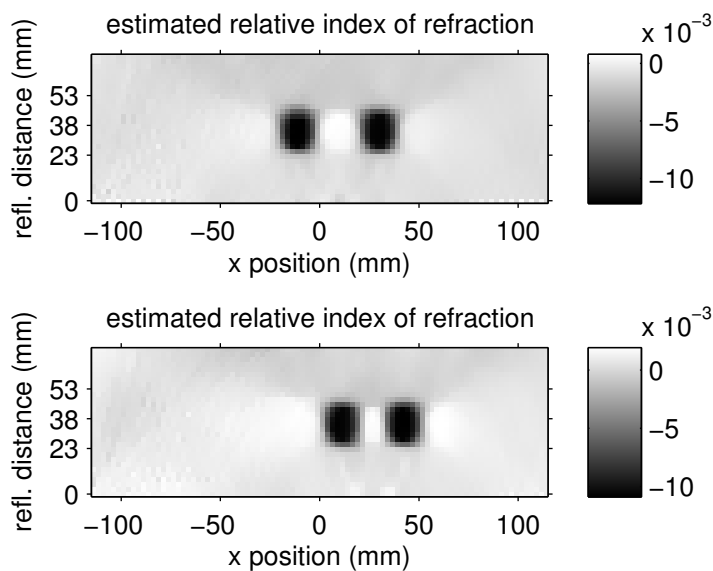


Figure 6. Reconstruction of pair-of-hole images; (top) with centers 4cm apart, (bottom) with centers 3cm apart.

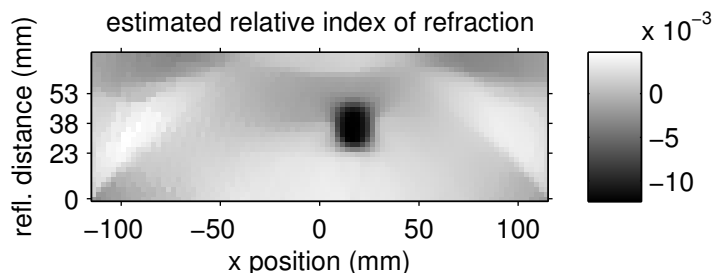


Figure 7. Reconstruction of center hole without k correction.